Speckle-Based X-Ray Phase-Contrast and Dark-Field Imaging with a Laboratory Source

I. Zanette,[1*] T. Zhou,[2] A. Burvall,[2] U. Lundström,[2] D. H. Larsson,[2] M. Zdora,[1] P. Thibault,[3] F. Pfeiffer,[1] and H. M. Hertz[2]
[1]*Physik-Department, Technische Universität München, Garching 85748, Germany*
[2]*Department of Applied Physics, KTH Royal Institute of Technology, Stockholm 106 91, Sweden*
[3]*Department of Physics & Astronomy, University College London, London WC1E 6BT, United Kingdom*
(Received 19 March 2014; published 26 June 2014)

We report on the observation and application of near-field speckles with a laboratory x-ray source. The detection of speckles is possible thanks to the enhanced brilliance properties of the used liquid-metal-jet source, and opens the way to a range of new applications in laboratory-based coherent x-ray imaging. Here, we use the speckle pattern for multimodal imaging of demonstrator objects. Moreover, we introduce algorithms for phase and dark-field imaging using speckle tracking, and we show that they yield superior results with respect to existing methods.

DOI: 10.1103/PhysRevLett.112.253903 PACS numbers: 42.30.Ms, 42.30.Rx, 52.59.Px, 87.59.-e

X-ray phase-contrast and dark-field imaging methods are investigated worldwide to overcome the limitations of conventional absorption imaging and access unprecedented and complementary object information. More specifically, phase-contrast imaging is often more sensitive than absorption imaging to minute density differences such as those between different types of soft tissue [1], whereas dark-field imaging provides a map of the scatter strength from unresolvable features in the specimen, such as nanopores, cracks, or fibers [2]. These imaging methods have tremendous potential in many application areas, including biomedical imaging, security screening, and materials science. However, access to phase-contrast and dark-field imaging remains impractical because these methods often require complicated setups and stringent requirements on the properties of the x-ray beam. Among the various x-ray phase-contrast imaging techniques developed in the last decades [3–6], only propagation-based methods and grating-based methods are tolerant to divergent and polychromatic beams, and hence compatible with laboratory x-ray sources [7–10].

Propagation-based methods use free-space propagation to generate an edge-enhanced image where the second derivative of the phase is superimposed to the absorption signal. They do not require a complex setup or sophisticated optical elements, and they can provide high-resolution data [7]. However, separation of the phase from the absorption information is often difficult or even impossible from propagation-based data, and the dark-field signal cannot be accessed. Grating-based methods, on the other hand, have multicontrast capabilities providing three complementary images from the same data set: the differential phase image, the dark-field image, and the absorption image. These methods, however, often rely on the use of two or three gratings placed between the source and the detector. These are microstructures which absorb radiation, thus causing an increase in the acquisition time [8–10].

More recently, a new class of phase-contrast imaging techniques has been introduced. Based on the analysis of sample-induced distortions of a near-field speckle pattern, these methods combine the simplicity of propagation-based imaging with the multiple contrast possibility of grating-based methods [11–13]. The speckles are typically generated by a random object with small structures, such as a piece of sandpaper or cardboard, and are resolved by an imaging detector [14]. However, while the properties of the speckle pattern do not crucially depend on the temporal coherence of the x-ray beam—as discussed, e.g., in Ref. [11]—up until now, speckle-based imaging methods have been implemented only at synchrotron facilities using monochromatic x-rays. The various speckle-based techniques differ for the data acquisition and analysis procedures, and the nature of the signal retrieved in the final images.

Single-shot speckle tracking [11] is a fast method which does not require a high-precision scanning stage and yields the refraction angles along two orthogonal directions. The advantage of fast acquisitions comes, however, at the cost of reduced spatial resolution, which is typically lower than the size of the speckles.

To increase the spatial resolution in the retrieved data, and perform a pixel-wise analysis of the speckle structures, a speckle-scanning method has been proposed [12]. This technique, however, requires a large number (more than 1000 in Ref. [12]) of images recorded at different lateral positions of the random object which is scanned in tiny steps smaller than the speckle size.

The most recent method, named "near-field ptychography," uses a ptychographic algorithm to analyze speckle patterns recorded at different (at least four) lateral positions of the specimen [13]. It allows direct reconstruction of the phase shift induced by the specimen simultaneously with the complex-valued illumination function. This makes near-field ptychography a robust method against beam

instabilities, and a reliable technique for accurate quantitative phase measurements.

In this Letter, we report on the observation of near-field speckles with a laboratory x-ray source, and we present the implementation of speckle-based multimodal imaging in this arrangement, using the single-shot speckle-tracking technique. Moreover, we describe new algorithms to retrieve the dark-field information and the quantitative phase image from the speckle data.

The experimental setup is schematically represented in Fig. 1(a). The x-ray generator was a liquid-metal-jet source with a Ga/In/Sn alloy as the electron-beam target [15]. It was operated at 50 kV and 30 W, and had a focal spot size of $7.8 \times 8.7\ \mu\text{m}^2$. The enhanced brilliance properties of this source have been exploited for propagation-based phase-contrast imaging with high resolution and high contrast [16,17]. The detector, located at $d = 3.00$ m from the source, was a CCD camera with an effective pixel size $p_s = 9.0\ \mu$m coupled through a fiber-optic plate to a 15-μm-thick 5 mg/cm^2 Gadox scintillator. The estimated mean x-ray energy of the detected photons was 16 keV (see Supplemental Material [18]).

The speckle pattern was generated by a piece of sandpaper at a distance $d_0 = 1.00$ m from the source [19]. The samples, a polyoxymethylene (POM) wedge and a plastic flower, were placed downstream of the sandpaper, at approximately $d_1 = 1.15$ m from the source. This geometry gave a magnification factor of 2.6 and a pixel size at the sample plane of 3.5 μm. Five images with an exposure time of 60 s each were collected for each sample, and five reference images were recorded without any sample in the beam path with the same exposure time. The five images in each group were averaged prior to analysis.

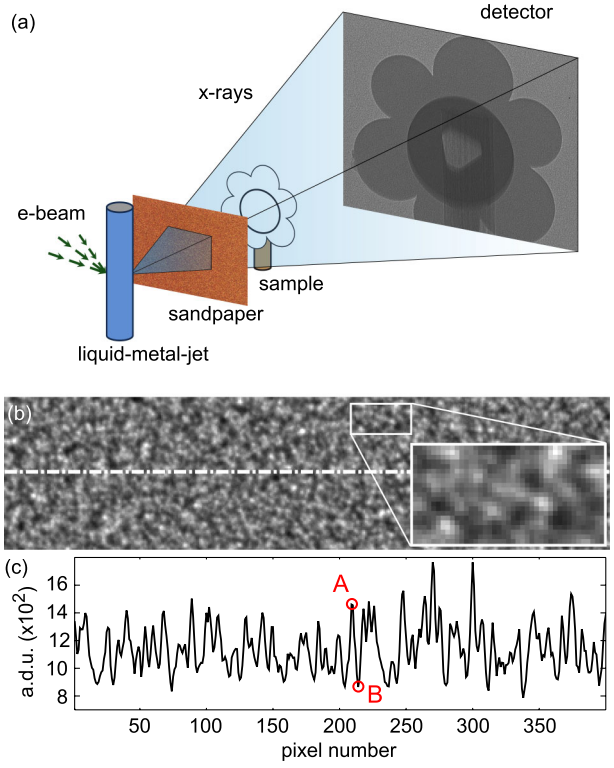

FIG. 1 (color online). (a) Setup for speckle-based x-ray imaging. (b) Near-field speckle pattern and (c) profile taken along the dashed line in (b). The y axis in panel (c) is the intensity recorded by the detector in arbitrary units (a.d.u.). The 40×20-pixel inset in (b) provides an enlarged view of the speckles.

The near-field speckle pattern recorded in this way is displayed in Fig. 1(b). The inset provides an enlarged view of the speckle structure and shows that their size at the detector plane is of approximately 6 pixels (50–60 μm). A profile taken along the dashed line in Fig. 1(b) is plotted in Fig. 1(c) and is used to estimate the speckle contrast. The visibility calculated from points A and B is $V = (I_A - I_B)/(I_A + I_B) = 31\%$.

A sample in the beam path modifies the near-field speckles in three ways: (i) the absorption in the sample decreases the transmitted intensity, (ii) the refraction causes a displacement of the speckles, and (iii) the scattering from unresolvable structures decreases the visibility of the speckles (dark-field signal).

Under the assumption of small refraction angles (which is essentially always valid in this type of experiments), the refraction angles along x and y, α_x and α_y, are proportional to the displacement field δ_x and δ_y caused by the sample: $\alpha_{x,y} = \delta_{x,y}/(d - d_1)$. Assuming that the sample features vary slowly compared to the speckles, and neglecting for the moment the dark-field signal, the measured speckle-and-sample image at a given point can be modeled by $\hat{I}(x, y) = TI_r(x - \delta_x, y - \delta_y)$, where T is the transmission of the sample and I_r is the speckle-only measurement. The values of T, δ_x, and δ_y can be extracted from the cost function

$$f(x_0, y_0; \delta_x, \delta_y, T) = \int [TI_r(x - \delta_x, y - \delta_y) - I(x, y)]^2 \times w(x - x_0, y - y_0)dxdy, \quad (1)$$

as described in the Supplemental Material [18]. In Eq. (1), $I(x, y)$ is the measured speckle-and-sample data, and w is a window function that masks all but a small region of the speckle image centered at (x_0, y_0). The quantities extracted from Eq. (1) vary spatially since the minimization is carried out for all possible translations (x_0, y_0) of the window w. The extent of the window w is an important parameter in the analysis, since larger windows provide a more accurate evaluation of the displacement field, at the expense of spatial resolution. In our analysis we used a window with size 24×24 pixels [20].

The results of this analysis are presented in Fig. 2. The transmission image in Fig. 2(a) shows the superposition of the absorption and the edge-enhancement signals. The latter appears as a bright line at the interface between

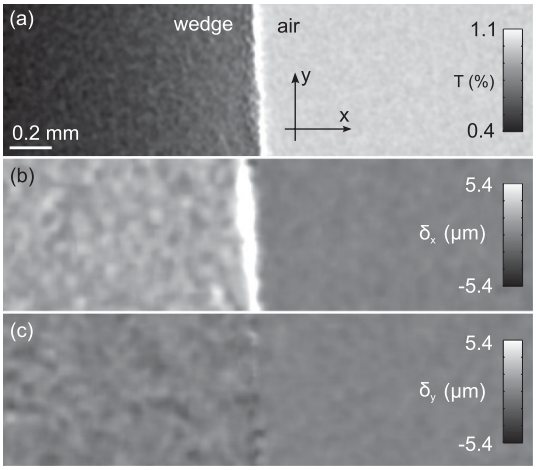

FIG. 2. Transmission image (a), and images of the displacements along x (b) and y (c) of the near-field speckles caused by a plastic wedge.

the plastic and air. The measured speckle displacements along x and y are shown in Figs. 2(b) and 2(c), respectively. As expected, the speckles are shifted mostly in the horizontal direction. The value of δ_x is constant throughout the wedge, except at its edge where it increases to more than 5 μm. This might indicate that the angle of the wedge is much larger than 45 degrees in that region. Testing experimental data against theoretical values, we observe that the displacement of the speckles calculated in a region of interest of 100×100 pixels centered in the wedge is $\delta_x = 1.80 \pm 0.45$ μm. This corresponds to $\alpha_x = 0.99 \pm 0.24$ μrad. For a 45-degree wedge, the refraction angle in the wedge direction is equal to δ, the real part of its refractive index. This can be derived from the relation $\alpha_x(x,y) = \partial_x \phi(x,y)/k$, where $k = 2\pi/\lambda$ with λ the wavelength of the radiation, $\phi(x,y)$ is the phase shift $\phi(x,y) = -k\delta t(x,y)$, and $t(x,y)$ indicates the thickness of the specimen. For a 45-degree wedge in the geometry of the experiment $t(x,y) = -x + \text{const}$. According to the value calculated from the NIST database [23], the measured value of $\delta = 0.99 \pm 0.24 \times 10^{-6}$ for POM corresponds to an effective x-ray energy in the interval 16–20 keV; this is slightly higher than the mean energy of the spectrum without the sample, and is probably also due to beam hardening. The vertical displacement computed from Fig. 2(c) of $\delta_y = 0.09 \pm 0.24$ μm confirms that no refraction along y could be observed.

The second sample imaged in this study was a plastic flower glued on a wooden rod; see Fig. 3. The absorption image in Fig. 3(a) shows the petals, a central thicker disc with a hole in the middle, and the wooden rod used as support. The refraction angle images along x and y are shown in Figs. 3(b) and 3(c), respectively. The presence of vertical structures (wood fibers) in the wooden rod creates a strong differential phase signal along x [Fig. 3(b)], while almost no contrast from the wooden rod can be seen in Fig. 3(c). This wooden support contains small scattering structures which strongly reduce the visibility of the speckles as visible in the dark-field image, Fig. 3(d).

Here, we obtain the dark-field signal D by including the speckle contrast in the model used to retrieve the refraction angle data. When the speckle visibility is taken into account, the speckle-only signal can be decomposed into its average I_0 and its spatial fluctuation ΔI_r: $I_r(x,y) = I_0 + \Delta I_r(x,y)$. The dark-field signal D, with values between 0 and 1, enters the model as $\hat{I}(x,y) = T[I_0 + D\Delta I_r(x-\delta_x, y-\delta_y)]$, and the cost function becomes

$$f(x_0,y_0;\delta_x,\delta_y,T,D) = \int \{T[I_0 + D\Delta I_r(x-\delta_x,y-\delta_y)] - I(x,y)\}^2 \times w(x-x_0,y-y_0)\,dx\,dy. \quad (2)$$

As for T, the quantity D can be analytically calculated from Eq. (2) by solving $\partial f/\partial D = 0$ (see Supplemental Material [18]).

With respect to previous works on speckle-based imaging, where the dark-field signal has been computed as the standard deviation of the speckle data [12], this method is based on a physical model that treats in a realistic way the decoherence effects of small scattering structures.

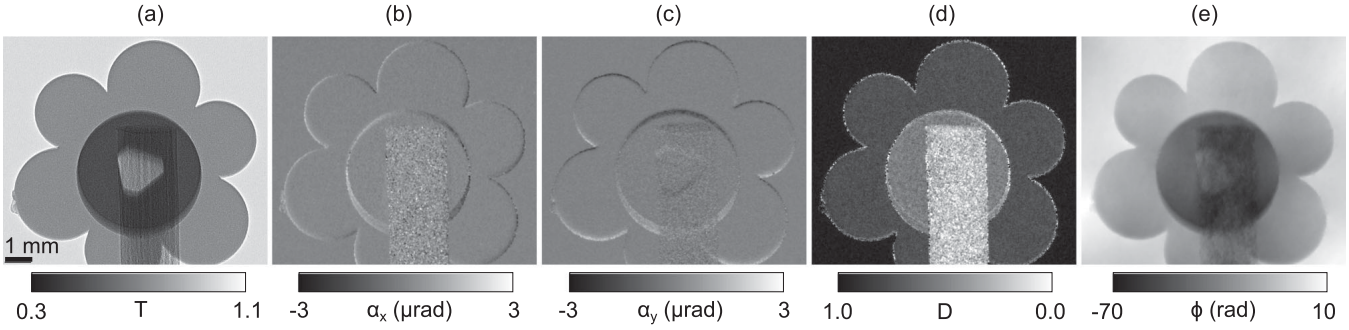

FIG. 3. Speckle-based multimodal images of a plastic flower on a wooden rod. (a) transmission, (b) refraction along x, (c) refraction along y, (d) dark-field, and (e) phase shift.

Moreover, we introduce a method to exploit the value of the cost function in Eq. (2) at its minimum, $f_{\min}$, to obtain a reliable reconstruction of the phase image. In particular, the value $f_{\min}$ has been used as an estimation of the quality of the data (lower $f_{\min}$ values correspond to better quality measurements) to weight different regions of the image. The quantitative phase image obtained with our regularized finite-difference method is shown in Fig. 3(e). Further information on this integration method is given in the Supplemental Material [18], where the superiority of this integration technique over the commonly used Fourier integration (see, e.g., Ref. [11]) is also demonstrated. The quantitativeness of the phase shift calculated in this way is confirmed by comparing the refractive index of the 800 μm-thick petals to the theoretical phase shift. The experimental value of $\delta = 1.48 \times 10^{-6}$, obtained from the average phase shift of -10 rad in the petals, is consistent with the refractive index of plastic materials at 16 keV [23].

It should be noted that the algorithms presented here are not limited to speckle-based x-ray imaging, but can be extended and applied to any other differential phase-contrast and/or dark-field imaging method, e.g., visible-light microscopy.

The access to the quantitative phase profile of the x-ray wave front from speckle data suggests the possibility of using this technique for wave-front characterization and metrology experiments at laboratory sources [24]. The dark-field signal obtained from speckle data is isotropic and not directional, as in some grating-based methods. Speckle-based imaging might therefore become a powerful tool for the detection of (among others) pathological breast tissues, which are often characterized by strongly oriented features [25].

Furthermore, the study of the visibility evolution of the near-field speckle pattern along the optical axis might be used as a reliable measurement of the coherence properties of the x-ray beam, as reported from experiments performed at synchrotrons [26,27]. Finally, it is also possible to use the information from near-field speckles for studies of colloids or complex fluids with a laboratory setup [28].

We acknowledge financial support from the DFG Cluster of Excellence Munich-Centre for Advanced Photonics (MAP), the DFG Gottfried Wilhelm Leibniz program, and the European Research Council (ERC, FP7, StG 240142 & 279753), the Swedish Research council, and the Wallenberg foundation. We acknowledge Hongchang Wang for fruitful discussions.

*irene.zanette@tum.de

[1] R. Fitzgerald, Phys. Today **53**, No. 7, 23 (2000).
[2] F. Pfeiffer, M. Bech, O. Bunk, P. Kraft, E. F. Eikenberry, C. Brönnimann, C. Grünzweig, and C. David, Nat. Mater. **7**, 134 (2008).
[3] A. Momose, T. Takeda, Y. Itai, and K. Hirano, Nat. Med. **2**, 473 (1996).
[4] V. N. Ingal and E. A. Beliaevskaya, J. Phys. D **28**, 2314 (1995).
[5] P. Cloetens, W. Ludwig, J. Baruchel, D. Van Dyck, J. Van Landuyt, J. P. Guigay, and M. Schlenker, Appl. Phys. Lett. **75**, 2912 (1999).
[6] A. Momose, S. Kawamoto, I. Koyama, Y. Hamaishi, K. Takai, and Y. Suzuki, Jpn. J. Appl. Phys. **42**, L866 (2003).
[7] S. W. Wilkins, T. E. Gureyev, D. Gao, A. Pogany, and A. W. Stevenson, Nature (London) **384**, 335 (1996).
[8] F. Pfeiffer, T. Weitkamp, O. Bunk, and C. David, Nat. Phys. **2**, 258 (2006).
[9] H. Wen, E. E. Bennett, M. M. Hegedus, and S. Rapacchi, Radiology **251**, 910 (2009).
[10] P. C. Diemoz, M. Endrizzi, C. E. Zapata, Z. D. Pesic, C. Rau, A. Bravin, I. K. Robinson, and A. Olivo, Phys. Rev. Lett. **110**, 138105 (2013).
[11] K. S. Morgan, D. M. Paganin, and K. K. W. Siu, Appl. Phys. Lett. **100**, 124102 (2012).
[12] S. Berujon, H. Wang, and K. Sawhney, Phys. Rev. A **86**, 063813 (2012).
[13] M. Stockmar, P. Cloetens, I. Zanette, B. Enders, M. Dierolf, F. Pfeiffer, and P. Thibault, Sci. Rep. **3**, 1927 (2013).
[14] R. Cerbino, L. Peverini, M. A. C. Potenza, A. Robert, P. Bosecke, and M. Giglio, Nat. Phys. **4**, 238 (2008).
[15] O. Hemberg, M. Otendal, and H. M. Hertz, Appl. Phys. Lett. **83**, 1483 (2003).
[16] T. Tuohimaa, M. Otendal, and H. M. Hertz, Appl. Phys. Lett. **91**, 074104 (2007).
[17] U. Lundström, D. H. Larsson, A. Burvall, L. Scott, U. Westermark, M. Arsenian Henriksson, and H. M. Hertz, Phys. Med. Biol. **57**, 7431 (2012).
[18] See Supplemental Material at http://link.aps.org/supplemental/10.1103/PhysRevLett.112.253903, which includes Refs. [21,22].
[19] The sandpaper had a granularity of *P*800 according to the FEPA *P*-grit classification for coated abrasives. This corresponds to a mean SiC grain size of 21.8 ± 1.0 μm. The grains are fixed on a cellulose backing layer.
[20] To determine the window size, we have considered the standard deviation of the grey levels in a uniform region of interest of 100×100 pixels in the retrieved refraction angle images. The standard deviation in this region significantly decreases by increasing the window size until w reaches a size of 24×24 pixels. By further increasing the window size, we did not observe any significant improvement in the noise level, but only a worsening in spatial resolution. For this reason a window of 24×24 pixels has been selected as optimal for our analysis.
[21] O. Axelsson, *Iterative Solution Methods* (Cambridge University Press, Cambridge, England, 1996).
[22] C. Kottler, C. David, F. Pfeiffer and O. Bunk, Opt. Express **15** 1175 (2007).
[23] B. L. Henke, E. M. Gullikson, and J. C. Davis, At. Data Nucl. Data Tables **54**, 181, (1993).
[24] S. Bérujon, E. Ziegler, R. Cerbino, and L. Peverini, Phys. Rev. Lett. **108**, 158102 (2012).

[25] M. Stampanoni, Z. Wang, T. Thüring, C. David, E. Roessl, M. Trippel, R. Kubik-Huch, G. Singer, M. Hohl, and N. Hauser, Investigative Radiology **46**, 801 (2011).

[26] F. Pfeiffer, O. Bunk, C. Schulze-Briese, A. Diaz, T. Weitkamp, C. David, J. F. van der Veen, I. Vartanyants, and I. K. Robinson, Phys. Rev. Lett. **94**, 164801 (2005).

[27] M. D. Alaimo, M. A. C. Potenza, M. Manfredda, G. Geloni, M. Sztucki, T. Narayanan, and M. Giglio, Phys. Rev. Lett. **103**, 194805 (2009).

[28] F. Ferri, D. Magatti, D. Pescini, M. A. C. Potenza, and M. Giglio, Phys. Rev. E **70**, 041405 (2004).